Chin. J. Astron. Astrophys. Vol. 4 (2004), No. 5, 440–454
(http://www.chjaa.org or http://chjaa.bao.ac.cn)

Chinese Journal of Astronomy and Astrophysics

Molecular Gas and Dust in the Massive Star Forming Region S 233 IR *

Rui-Qing Mao[1,2] and Qin Zeng[1]

[1] Purple Mountain Observatory, Chinese Academy of Sciences, Nanjing 210008; rqmao@jets.pmo.ac.cn
[2] National Astronomical Observatories, Chinese Academy of Sciences, Beijing 100012

Received 2004 February 2; accepted 2004 March 30

Abstract The massive star forming region S 233 IR is observed in the molecular lines CO $J = 2$–1, 3–2, NH_3 (1,1), (2,2) and the 870 μm dust continuum. Four submillimeter continuum sources, labelled SMM 1–4, are revealed in the 870 μm dust emission. The main core, SMM1, is found to be associated with a deeply embedded near infrared cluster in the northeast; while the weaker source SMM2 coincides with a more evolved cluster in the southwest. The best fit spectral energy distribution of SMM1 gives an emissivity of $\beta = 1.6$, and temperatures of 32 K and 92 K for the cold– and hot–dust components. An SMM1 core mass of 246 $M_\odot$ and a total mass of 445 $M_\odot$ are estimated from the 870 μm dust continuum emission. SMM1 is found to have a temperature gradient decreasing from inside out, indicative of the presence of interior heating sources. The total outflow gas mass as traced by the CO $J = 3$–2 emission is estimated to be 35 $M_\odot$. Low velocity outflows are also found in the NH_3 (1,1) emission. The non-thermal dominant NH_3 line width as well as the substantial core mass suggest that the SMM1 core is a "turbulent, massive dense core", in the process of forming a group or a cluster of stars. The much higher star formation efficiency found in the southwest cluster supports the suggestion that this cluster is more evolved than the northeast one. Large near infrared photometric variations found in the source PCS–IR93, a previously found highly polarized nebulosity, indicate an underlying star showing the FU Orionis type of behavior.

Key words: ISM: jets and outflows — ISM: molecules — ISM: dust, extinction — stars: formation — ISM: individual (IRAS 05358+3543; S 233 IR)

1 INTRODUCTION

Formation of massive stars has attracted increasing amount of interest in the past decade. While more and more observational results indicate that the basic picture of massive star

* Supported by the National Natural Science Foundation of China.

formation resembles in many aspects its low-mass counterpart, its early stage still remains a major unsolved problem and more individual cases need to be studied.

Recently we carried out a series of studies on the molecular lines and submillimeter dust emission of a sample of high-mass YSO candidates, based on their infrared color and flux (Mao 1999, 2004 in preparation). We present, in this paper, the results for one of the candidates, IRAS 05358+3543 ($\alpha_{2000} = 05^{\rm h}39^{\rm m}10.4^{\rm s}$, $\delta_{2000} = +35^\circ45'19''$, I 05358 hereafter).

In a $1^\circ \times 1^\circ$ optical image surrounding I 05358 (Fig. 1), there are four HII regions, of which the most prominent is S 235 located at approximately $25'$ east and $5'$ north of I 05358, and the smallest is S 233, closer to I 05358 (see also Porras et al. 2000, hereafter PCS). We adopt a widely used distance of 1.8 kpc for I 05358 and the associated star forming region (hereafter designated S 233 IR).

Infrared photometric studies revealed two distinct young stellar clusters. I 05358 is inside the SW cluster, while the more deeply embedded NE cluster is located at ∼0.5 pc northeast of I 05358 (Hodapp 1994; PCS). Two deeply embedded jet/counter–jet HH–like structures, produced by shocked H_2 gas, are detected near this NE cluster, in which a dense molecular core is revealed in CS (Cesaroni et al. 1999). Water masers and strong 6.7 GHz CH_3OH masers are detected in the center of the core (Tofani et al. 1995; Menten et al. 1991; Szymczak et al. 2000). Near infrared (NIR) K'–band polarization maps (Jiang et al. 2001) provide more evidence for a deeply embedded source (hereafter DES) inside the NE cluster. Although Snell et al. (1990) showed the CO $J = 1$–0 outflow with two overlapping lobes to be centered on I 05358, the most recent IRAM–30m CO $J = 2$–1 observations (Beuther et al. 2002a) found the outflow center to be close to the DES position, rather than I 05358. This is consistent with all the other observations. Furthermore, the high resolution observations (Beuther et al. 2002a) revealed a remarkable highly collimated and massive ($> 10\,M_\odot$) bipolar outflow, which forms part of a quadrupolar outflow system.

This paper presents the results of our observation of CO $J = 2$–1, 3–2, NH_3 (1,1), (2,2), and 870 μm submillimeter continuum image. The dust emission is also analyzed using the higher resolution (HIRES) maps of the Infrared Astronomical Satellite (IRAS) data. The properties of the outflowing gas, the dense gas and the cold dust will be deduced, and the process of star formation throughout the region, examined.

2 OBSERVATIONS

2.1 CO at KOSMA–3m

The CO observations were made in September and December 1998, using the 3m radiotelescope of the Kölner Observatorium für Sub-Millimeter Astrophysik (KOSMA) equipped with a dual channel SIS receiver. The half-power beamwidth of the telescope was $120''$ at the frequency of CO $J = 2$–1 (230.538 GHz) and $80''$ at that of CO $J = 3$–2 (345.796 GHz). An Acousto-Optical-Spectrometer (AOS) formed the backend, with a bandwith of 300 MHz and spectral resolutions of 0.5 and 0.3 km s^{-1}. All the results displayed are given on a main beam brightness temperature scale ($T_{\rm MB}$), which is related to $T_{\rm A}^*$ by $T_{\rm MB} = T_{\rm A}^*\ (F_{\rm eff}/B_{\rm eff})$ (see Downes 1989). The main beam efficiency, $B_{\rm eff}$, obtained from measurements of Saturn was 0.76 at 230 GHz and 0.72 at 345 GHz. The forward hemisphere efficiencies, $F_{\rm eff}$, were 0.92 and 0.93, respectively. The pointing was checked to be accurate within $10''$. Calibrations with an expected accuracy of about ±20% were made by observing Orion-KL before and after the mapping observation.

2.2 NH_3 Observations on the MPIfR–100m

The NH_3 observations were obtained in July 1999, using the Effelsberg 100-m telescope of MPIfR equipped with a maser receiver. Typical system temperature during our observations was about 110 K on the main beam brightness temperature scale; the half-power beamwidth was $40''$, and the observed spectral resolution was $0.24\,\mathrm{km\,s^{-1}}$. The line intensities were calibrated relative to NGC 7027, which we assumed to have a brightness temperature of 8.1 K. The pointing was checked to be accurate to within $\sim 5''$, and the calibration was expected to be accurate to about $\pm 20\%$.

2.3 870 μm Continuum Observation

The 870 μm dust continuum emission was imaged in May 2000, with the HHT 19 channel bolometer array in an On-The-Fly (OTF) mode. The array covered a hexagonal $200''$ field of view. The half-power beamwidth was $22''$. A wobbler throw of $120''$ and a scanning speed of $8''$ were used for the OTF mapping. The image was taken in a field of $400'' \times 300''$ centered on I 05358. The map was calibrated using 870 μm skydips to trace the atmospheric opacity and from standard calibrators Uranus and G34.3, and a peak flux density of 60 Jy was assumed for the latter. The typical atmospheric opacity at 870 μm was about 0.4 during the observation. The rms noise level was about 150 mJy. The calibration accuracy was expected to be $\pm 20\%$.

3 RESULTS

3.1 Infrared Properties

3.1.1 Far and Mid Infrared

We retrieved the HIRES maps of a $1^\circ \times 1^\circ$ region centered on I 05358 in the four IRAS bands (i.e., 12, 25, 60 and 100 μm) and also the 8–25 μm mid-infrared (MIR) data of the same region from the Midcourse Space Experiment (MSX) Point Source Catalog.

Figure 1 presents the HIRES 100 μm contours, overlaid on the 2nd generation digitized sky survey (XDSS) optical image of a $1^\circ \times 1^\circ$ region surrounding I 05358. While S 235 and S 233 are well associated with the 100 μm emission, there is no obvious associated far infrared dust emission. Next to the bow-shock-like HII region S 231, the 100 μm emission forms a dust envelope nicely attached to the cometary front of S 231. This dark dust feature is shown in all the four IRAS bands as well as the MSX 8 μm image. The MSX 8 μm image (not shown here) looks very much like the HIRES 100 μm image on large scale.

Figure 2 shows the 20-iteration HIRES results of I 05358 in the four IRAS bands. The intensity peaks in the four bands are at ($-15''$, $0''$), ($30''$, $30''$),($44''$, $30''$), ($45''$, $30''$), respectively. As has been pointed out by Beuther et al. (2002a), the disagreement of the peak at 12 μm with the other bands indicates the embedded nature of the sources in the NE cluster and the more evolved nature of I 05358. Strong evidence for this scenario is provided by the four-band MSX images around I 05358 (Fig. 3) . While the emission is prominent close to I 05358 at 8–15 μm, another almost equally strong peak shows up at ($33''$, $28''$) in the 20 μm image, which coincides with the HIRES 25 μm peak position. This can also be inferred from the elongated structure of IRAS 25 μm emission (see Fig. 2), which could well be fitted by two Gaussian components peaked at ($30''$, $30''$) and ($0''$, $0''$), respectively. The integrated flux densities at 12, 25, 60 and 100 μm, estimated from the HIRES data are 2.0, 33.7, 449 and 975 Jy, which give a bolometric luminosity of $3.7 \times 10^3\,L_\odot$.

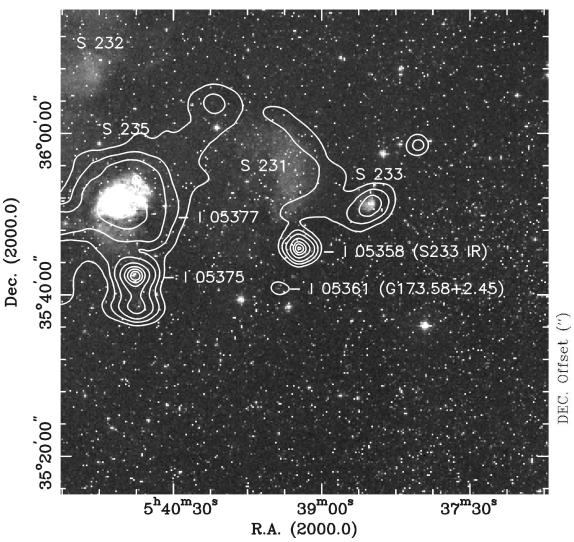

Fig. 1 HIRES 100 μm contours (20 iterations) overlaid on the DSS image. The contour levels are 2, 4, 8, 20, 40, 60, 80% of the peak value (=5280 MJy sr^{-1}). Labelled are the four HII regions and four IRAS sources mentioned in the text.

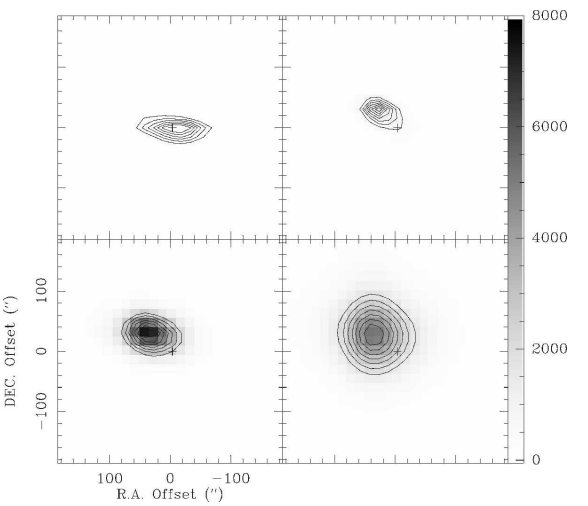

Fig. 2 HIRES four band contours and grey–scale images (20 iterations) towards I 05358. The contour levels are 30, 40, ..., 90% of the peak values, which are 98, 1780, 7513 and 5289 MJy sr^{-1} at the 12, 25, 60 and 100 μm bands, respectively. The grey–scale wedge is labelled in units of MJy sr^{-1}. A plus sign marks the position of I 05358.

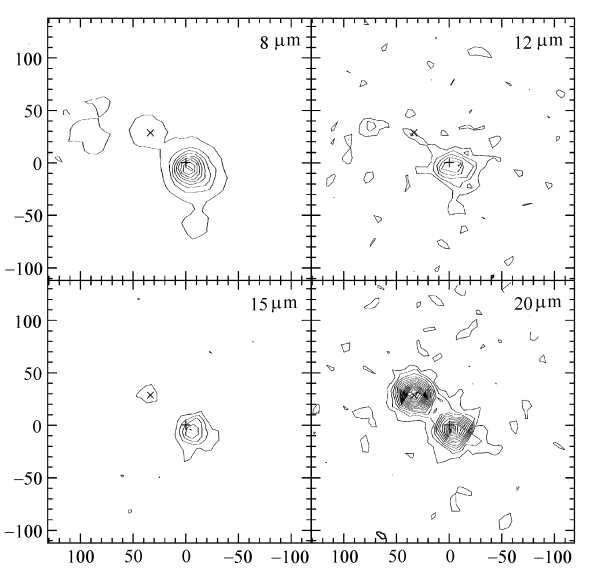

Fig. 3 Four-band MSX contours zoomed around I 05358. The lowest counter level is 2×10^{-6} W m^{-2} sr^{-1} at all four bands and the contour intervals are 2×10^{-6} W m^{-2} sr^{-1} for bands C (12.13 μm) and D (14.65 μm), and 4×10^{-6} W m^{-2} sr^{-1} for bands A (8 μm) and E (21.34 μm). Symbols '+' and '×' mark the positions of I 05358 and the HIRES 25 μm peak (30″, 30″), respectively.

3.1.2 Near Infrared

Stars within 8′ diameter of I 05358 are extracted from the Two Micron All Sky Survey (2MASS) catalog which contains the $J(1.25\,\mu\mathrm{m})$, $H(1.65\,\mu\mathrm{m})$ and $K_\mathrm{s}(2.17\,\mu\mathrm{m})$ magnitudes of the stars. Completeness limits in magnitude are close to 17, 16 and 15 mag in the J, H and K_s bands, respectively.

The PCS detected 98 stars in a 3.1′×3.1′ region (corresponding to 1.6 pc×1.6 pc at 1.8 kpc) around I 05358. We examine the 2MASS JHK$_s$ photometric data of the same region. Of the 98 PCS stars 74 are detected in at least one 2MASS band, 64 in at least two bands and 46 in all three bands. In addition, there are four stars (See Table 1) newly detected in the 2MASS (in at least two bands) that are not in the PCS. The color–color diagram looks quite similar to the one shown in the PCS, so we do not show it here.

Table 1 Newly Detected 2MASS Sources

Source	α_{2000} (h m s)	δ_{2000} (° ′ ″)	J (mag)	H (mag)	K (mag)
1	05 39 09.1	35 45 18.4	–	15.30±0.13	14.21±0.09
2	05 39 09.1	35 45 26.2	16.82±0.18	15.28±0.10	14.64±0.09
3	05 39 19.1	35 46 51.2	16.47±0.10	14.36±0.04	13.51±0.04
4	05 39 05.7	35 47 03.0	–	16.22±0.18	13.87±0.05

To investigate the variability of the stars, we made a comparison of photometric data between PCS (January 1997) and 2MASS (January 1998 as given in the FITs header). The mean differences (PCS – 2MASS) in three bands, $\langle\Delta J\rangle$, $\langle\Delta H\rangle$ and $\langle\Delta K\rangle$, are 0.19, 0.21 and 0.26, respectively. To avoid possible confusion from photometric errors, we set the following criteria for variable star: the variation should 1) be found in at least two bands; 2) show the same trends (decrease or increase) in all the bands; 3) satisfy $|\Delta\, m_\mathrm{i}| \geq 0.5$ in at least one band. We found seven stars that satisfied these criteria; their variations are listed in Table 2, in which we retain the source name from PCS for the sake of comparison. For interest, we have noticed that the photometric differences are very small for PCS–IR41 (the counterpart of I 05358, $\langle\Delta J\rangle$=–0.10±0.04, $\langle\Delta H\rangle$ =–0.12±0.06 and $\langle\Delta K\rangle$=0.09±0.12).

Table 2 Photometric Differences ($m_\mathrm{PCS} - m_\mathrm{2MASS}$)

Source	$\Delta\, J$ (mag)	$\Delta\, H$ (mag)	$\Delta\, K$ (mag)
PCS–IR 2	–1.60±0.05	–1.52±0.06	–1.57±0.08
PCS–IR 3	1.48±0.04	1.61±0.03	1.63±0.07
PCS–IR 39	0.66±0.16	0.19±0.11	–
PCS–IR 40	1.08±0.17	0.56±0.15	–
PCS–IR 62	–	0.48±0.11	0.77±0.10
PCS–IR 81	1.19±0.22	1.71±0.24	1.10±0.23
PCS–IR 93	–	1.07±0.16	1.48±0.28

3.2 Outflow

Both the CO $J = 3$–2 and 2–1 emissions were mapped in a region of $8' \times 8'$ around I 05358. Broad-line wing emission was detected in both maps. The line wing is defined by comparing the spectral profile of the $J = 3$–2 transition at the peak position (40″, 40″) and an average profile

of the spectra at the four corners ($\pm160''$, $\pm160''$). Since these four corners are mostly free of the outflow emission, an average of the four spectra may hopefully avoid possible contamination by velocity shifts induced by rotations and/or infall motions of the clouds. In this way we defined the outflow in velocities redder than –14 km s^{-1} or bluer than –21 km s^{-1}. Emission of the two CO transitions shows a very similar outflow structure. Figure 4 presents only the higher angular resolution CO J = 3–2 map. The blue- (–31 to –21 km s^{-1}) and the red-shifted (–14 to –3 km s^{-1}) lobes are shown in solid and dashed contours, respectively. However, the overall outflow morphology resembles the previous CO J =1–0 map (Snell et al. 1990), our map, with an even lower resolution, shows that the two overlapping lobes are centered close to the dense core region but not on the IRAS position. This is consistent with high resolution results from Beuther et al. (2002a) and the observations of Snell et al. (1990) likely suffered from a pointing problem. The position velocity map along the declination axis is presented in Fig. 5 in which the outflow emission is again evident. The CO spectra were peaked at a velocity of about –18 km s^{-1}, and the red-shifted emission is more prominent than the blue-shifted emission.

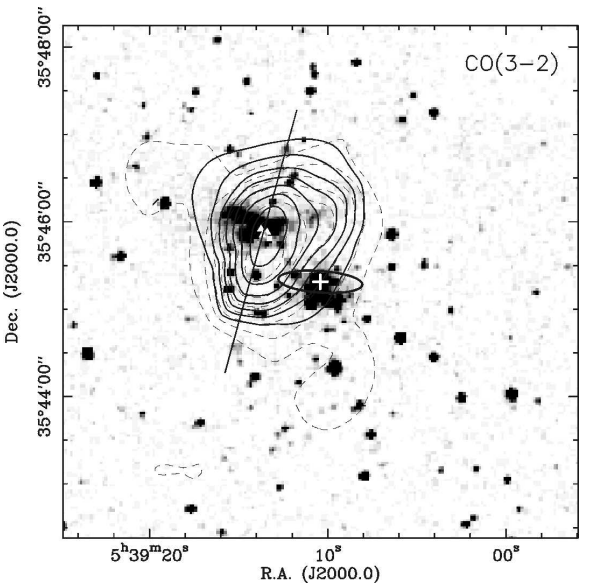

Fig. 4 CO(3–2) outflow (contours) of the S 233 IR overlaid on the 2MASS-K$_s$ image (grey). The red-shifted (dashed) and the blue-shifted (solid) emissions are integrated from –14 to -4 km s^{-1}and –31 to –21 km s^{-1}, respectively. Contour levels are 30%, 40%, ..., 90% of the peak value, (17 K km s^{-1} for the blue, 31 K km s^{-1} for the red). The cross marks the position of I 05358 position and the ellipse, the 1σ error ellipse. Triangles mark the water maser spots. Small crosses, the observed CO positions. The straight line indicates the direction of one of the H_2 jets (Porras et al. 2000).

3.3 870 μm Dust Emission

The 870 μm continuum image of this region is shown in Fig. 6. Its general morphology consists of a core-like condensation surrounded by a much more diffused envelope-like structure. As expected, the peak appears at ($32''$, $31''$) with respect to I 05358, i.e. close to the 100 μm peak. The Gaussian core is unresolved with a deconvolved half power size of $21''\times19''$. We name this main core SMM1. Extending from SMM1 are two weak emission spurs, one to the

southwest (SMM2) and one to the northwest (SMM3 and SMM4). SMM2 is associated with I 05358. In fact, a recent 1200 μm continuum image (Beuther et al. 2002b), with an angular resolution of 11″, showed more clearly a sub–source close to I 05358. Beuther et al. (2002a) proposed that this sub-source is a remnant of an older cluster in which I 05358 was located. Much longer than the southwestern extension is the northwestern extension, in which we can distinguish two peaks, SMM3 and SMM4 (see Fig. 6). The 870 μm peak flux densities are 6.75, 1.6, 1.7 and 1.1 Jy beam^{-1} for SMM1, SMM2, SMM3 and SMM4, respectively. Integration over a 2–D Gaussian fit of SMM1 gives it a core flux of 20.0 Jy. For the other components, we estimate their flux densities by simply drawing polygons covering the emission. Flux densities of 3.6, 2.2 and 2.7 Jy are estimated for SMM2, SMM3 and SMM4, respectively. A total flux density of 36.2 Jy was obtained by integrating over the 3 σ level.

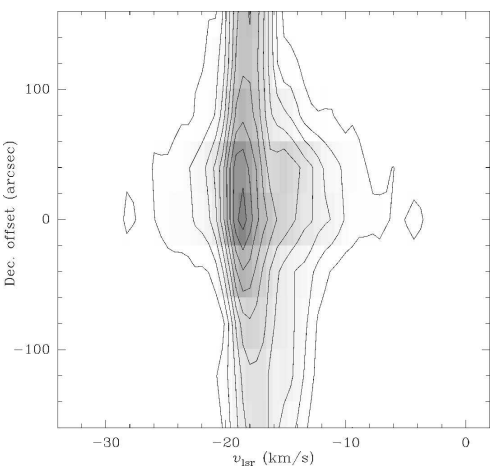

Fig. 5 Position versus velocity map along the Dec. axis at R.A. offset of 40″ relative to I 05358. The contours are from 0.8 K to 16 K in steps of 1.6 K.

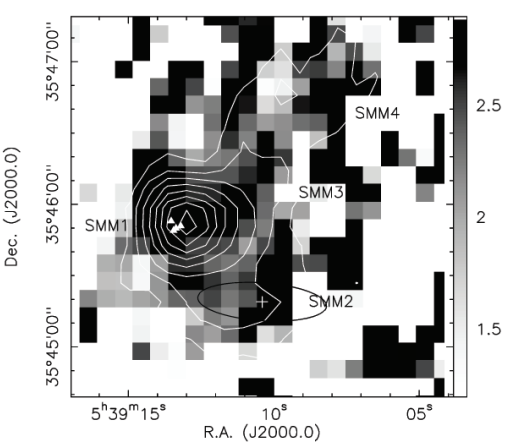

Fig. 6 HHT 870 μm dust continuum contours of S 233 IR overlaid on a grey scale map of the $F_{870\mu\rm m}/F_{1200\,\mu\rm m}$ ratio. The contours start at 0.6 Jy, and increment at steps of 0.8 Jy. Symbols have the same meaning as in Fig. 4.

3.4 Dense Molecular Gas

Strong NH_3 (1,1) and (2,2) emission were observed over a $1' \times 1.5'$ region around SMM1, with a peak T_{MB} of 3.7 K in (1,1) and 2.4 K in (2,2) towards the position (20″, 40″). V_{LSR} is about –16.3 km s^{-1} and the line width is 2.23 km s^{-1} at the peak position. Figure 7a displays the distribution of total integrated intensity (grey scales), and the red– (dashed contours) and blue–shifted (solid contours) emission of the NH_3 (1, 1) main group of lines. The morphology of the total integrated intensity map generally resembles that of the 870 μm dust emission, except it is smoother. The elongated clump in the SW-NE direction is most likely due to the spurs and the extended emission revealed in the 870 μm map. The deconvolved half-power beamwidth is 36″ (or 0.31 pc) in the shorter dimension and is more than 90″ (or 0.78 pc) in the longer dimension (the SW-NE direction), as it is not fully mapped.

All the positions detected in the (1,1) and (2,2) emission were analysed with a usual technique (see Harju et al. 1993). The rotation temperature T_{rot}, the column density $N(NH_3)$, and the number density $n(H_2)$ at the peak position (20″,40″) are calculated to be 21.5±1 K, $1.2\pm0.2\times10^{15}$ cm^{-2}, and $(3.4\pm0.6)\times10^4$ cm^{-3}, respectively. The T_{kin} corrected by the depopulation of lower energy levels, is $\geq 25.4\pm2$ K.

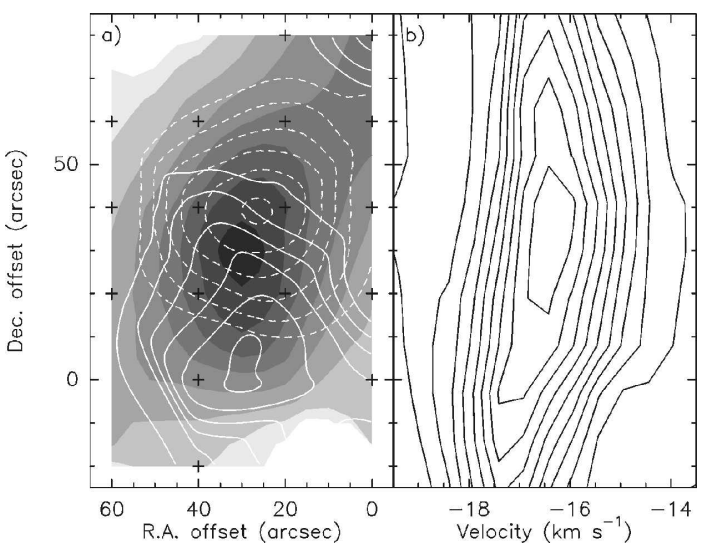

Fig. 7 (a) Blue– (–19.5 to –17.5 km s^{-1}) and red–shifted (–15.5 to –13.5 km s^{-1}) Effelsberg NH_3 contours overlaid on the total integrated main group of NH_3 (1,1) lines (grey scales). The contour levels are from 1.2 to 2.4 km s^{-1}at steps of 0.2 K km s^{-1}. All the observed positions are marked by plus signs. (b) The position–velocity diagram along the axis of R.A. offset = 30″. Contours are 10% to 90% by 10% of the peak value of 3.6 K.

4 DISCUSSION

4.1 Dust Properties: Temperatures and Emissivity

The flux density ratio can provide a good measure of dust temperature and emissivity. For a modified blackbody emission, the flux density at wavelength λ is $F_\lambda = B_\lambda(T_{dust})[1 - \exp(-\tau_\lambda)]\Omega_\lambda$, where τ_λ is the dust optical depth, $B_\lambda(T_{dust})$ is the Planck function at the dust

temperature $T_{\rm dust}$, and Ω_λ is the solid angle subtended by the dust–emitting region. For optically thin emission we can write $F_\lambda = B_\lambda(T_{\rm dust})\tau_\lambda\Omega_\lambda$. It is important to use images with the same resolution when generating the flux density ratio maps.

4.1.1 Large Scale

To study the large scale dust temperature distribution in this region, we have created a flux density ratio map from the ratio F_{60}/F_{100} of the HIRES 60 μm and 100 μm maps. We took the 20th iteration images at both wavelengths and convolved to an effective beam size of $2.6'\times1.8'$ (HPBW). For $\tau \propto \lambda^{-\beta}$ and $\Omega_{60} \approx \Omega_{100}$, the ratio F_{60}/F_{100} can be written as $R_{60/100} = (60/100)^{-(3+\beta)}[e^{T_{100}/T_{\rm dust}}-1]/[e^{T_{60}/T_{\rm dust}}-1]$, where $T_{\rm i} = hc/k\lambda_{\rm i}$ ($i = 60\,\mu$m, 100 μm), and $\beta = 1$ should be adopted for $\lambda = 60$ and 100 μm. The color correction of IRAS flux densities were taken into account (Beichmann et al. 1987, table VI.C.6). The highest dust temperatures ($\sim$50 K) are found in the north of S 235 and the lowest dust temperature ($\sim$30 K) in the dust envelope (see Sect. 3.1.1) in front of the S 231. A modest dust temperature of 38 K is found at the position of the 100 μm peak near I 05358.

4.1.2 Small Scale

Zooming into the region close to I 05358, where we have both the 870 μm and the 1200 μm continuum maps available, we convolve the 1200 μm map from Beuther et al. (2002b) with a gaussian to an effective beam size of $22''$ (HPBW), the resolution of our 870 μm map. The $R_{870/1200} = F_{870\,\mu{\rm m}}/F_{1200\,\mu{\rm m}}$ flux density ratio map is shown as grey scale in Fig. 6 (the darker the grey scale, the higher the ratio). Assuming that both the 870 μm and the 1200 μm emission are purely from the dust, tracing the same dust mass, a high ratio means either a high dust temperature at a given emissivity, or a higher emissivity at a given dust temperature. We will simply consider only the temperature effect in the following discussion. It is worth noting that in the ratio map we should only consider regions inside the lowest contour of the overlaid 870 μm map, since outside of that the low signal to noise ratio gives an artificially accentuated temperature distribution. The dust temperature in DES is apparently among the highest in the map with a ratio $R_{870/1200} = 2.97$ at a resolution of $22''$. Furthermore, we found that the ratio $R_{870/1200}$ gets lower when we smooth the maps down to a lower resolution, e.g., $R_{870/1200}$=2.67 at $40''$ resolution. This outward temperature gradient indicates the presence of interior heating sources. With the flux densities available from the infrared to the millimeter wavelengths, we investigated the spectral energy distribution (SED) to better constrain the dust temperature and the dust emissivity of the main core SMM1. Figure 8 shows the SED of the DES from 12 μm to 1.2 mm, which is mainly due to thermal dust emission. The peak values of the 20th iteration HIRES maps were taken for the IRAS flux densities at 25, 60 and 100 μm (solid triangles). The upper limits of the MSX flux densities (open squares) at bands C(12.13 μm) and D(14.65 μm) are indicated with arrows. For the 1200 μm (the open circle) and 870 μm (the solid star) flux densities, the peak values at $22''$ resolution are adopted. A single-temperature model produced poor fits, with the emission at λ<25 μm underestimated, and therefore a two temperature component model was applied. We adopted the angular size of $20''$ (HPBW) from our 870 μm map. The best fitting, shown by the dashed line in Fig. 8, gives a dust emissivity of β=1.6($\pm$0.2), and dust temperatures of 32($\pm$0.5) and 92($\pm$7) K for the cold– and hot–dust components, respectively. The dotted line gives only the colder component, which is the main contributor of the dust mass.

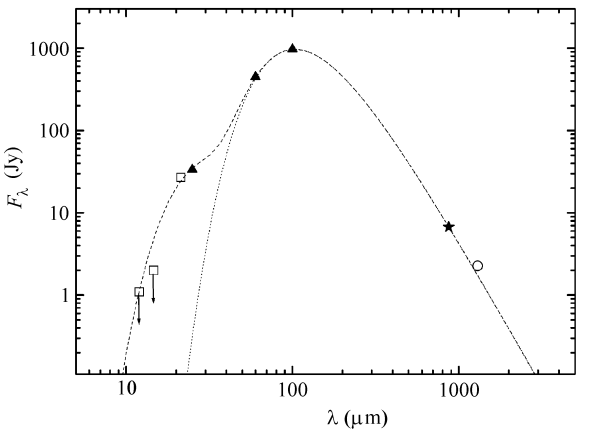

Fig. 8 Spectral energy distribution of S233–SMM1. The MSX, HIRES, IRAM 1200 μm and HHT 870 μm fluxes are shown as squares, triangles, a star and a circle, respectively. Arrows indicate upper limits. The best fit for the two temperature component greybody is given by the dashed curve and that for the cold component only, by the dotted curve.

4.2 Core Masses

The combined gas+dust masses of the cores can be estimated via $M = F_\nu \mathrm{D}^2/\kappa_\nu$ B $_\nu(T_\mathrm{d})$ (Hildebrand 1983), where F_ν is the flux density, D the distance to the cloud, $B_\nu(T)$ the Plank function for temperature T_d, and κ_ν the dust opacity per unit mass of gas and dust, which is frequency dependent; here $\kappa_\nu \propto \nu^\beta$. From the β fitted above, we derived the $\kappa_{870\,\mu m}$ and $\kappa_{1200\,\mu\mathrm{m}}$ to be 0.014 and $7.4{\times}10^{-3}$, respectively. According to Kerton et al. (2001) and the references therein, κ_{870} varies from 0.011 to 0.045 $\mathrm{cm^2\,g^{-1}}$ for dense cores, depending on the dust temperature and gas density. Our results are well within this range. The masses of the 870 μm peak and SMM1 are 84 $M_\odot$ and 246 $M_\odot$, respectively. We calculated also the beam averaged peak column density $N(\mathrm{H_2})$ to be $1.4{\times}10^{22}\,\mathrm{cm^{-2}}$ corresponding to an extinction of $A_\mathrm{v} \sim 150$ ($N(\mathrm{H_2}) = 0.95{\times}A_\mathrm{v}{\times}10^{21}\,\mathrm{cm^{-2}}$). The total mass, if we assume the same dust properties over the whole region, is then equal to 445 $M_\odot$.

The masses derived by Beuther et al. (2002b) was most likely an overestimate by a factor of $\sim$2.5 compared to our results. This is because that the value of κ_ν they took was extrapolated from the value at λ=125 μm, but according to Hildebrand (1983), we should use the value at λ=250 μm to extrapolate to wavelengths longer than 250 μm. Using the assumptions in Beuther et al. (2002b), we can obtain $\kappa_{870\,\mu\mathrm{m}}{=}3.87{\times}10^{-3}$ which falls well below the widely adopted range of $\kappa_{870\,\mu\mathrm{m}}$ mentioned above.

The mass can also be estimated from the NH_3 data. By smoothing the image to 40″, the resolution of NH_3 map, we can estimate a beam averaged (40″) column density $N(\mathrm{H_2})$ of about $6.9{\times}10^{22}\,\mathrm{cm^{-2}}$. Comparing the NH_3 peak column density derived in Sect. 3.3, we estimated the NH_3 abundance $\chi(\mathrm{NH_3})$ to be $\sim 1.7{\times}10^{-8}$, which is within the range of widely adopted values (e.g. Ho & Townes 1983). A clump thickness of 77″ (or 0.67 pc) can be estimated from the $N(\mathrm{H_2})$ and $n(\mathrm{H_2})$ (from Sect. 3.4). Since the region is not fully mapped, we take this value as a clump diameter for the mass calculation. The total clump mass was calculated to be about

$400\,M_\odot$. The virial mass derived from the line width is $414\,M_\odot$. Both are consistent with the mass derived from the dust emission.

4.3 Outflow Properties

From the ratio of Rayleigh-Jeans brightness temperatures for CO $J = 3$–2 and CO $J = 2$–1 (the 3–2 spectra were smoothed to the same spatial resolution of the 2–1 spectra here), we estimate the local thermodynamic equilibrium (LTE) excitation temperature $T_{\rm ex}$ of outflowing gas to be 20 K to 40 K for an extended source or 10 K to 14 K for a point source. We will take $T_{\rm ex}$=20 K in following outflow parameter calculations.

Assuming that the CO emission is near LTE and that the fractional abundance [CO] / [H_2]$\sim 10^{-4}$, we estimated the outflow parameters following a method introduced by Cabrit & Bertout (1990). From the integrated intensities of CO $J = 3$–2 emission, we estimated $1.2\,M_\odot$ and $2.6\,M_\odot$ for the blue– and red–shifted outflow lobes, or a total outflow mass of $3.8\,M_\odot$, assuming the high velocity gas to be optically thin. However, the opacity of high velocity gas emission is usually velocity dependent and can be as high as several tens at low velocities (Choi et al. 1993). Choi et al. (1993) found an average line wing ratio of ^{13}CO/^{12}CO$\sim$0.1 for seven massive star forming regions, assuming a constant ratio throughout the line wings. Taking this line wing ratio and a standard abundance ratio of [^{12}CO/^{13}CO] =89 into account, we can estimate the opacity corrected outflow masses of $11\,M_\odot$ and $24\,M_\odot$ for the blue– and red–shifted outflows, respectively, or $35\,M_\odot$ in total. These are higher than that from Beuther et al. (2002b), but within the uncertainties of mass determination that has been discussed by Cabrit & Bertout (1990). The outflow masses can be even higher if we consider the emission at low velocities since a significant amount of mass could be contained in the low velocity outflowing gas (e.g. Mao et al. 2002). In fact, we have already seen the low velocity outflow in NH_3 (see Sect. 4.4).

Given the lobe extension (after beam deconvolution) of 65″ (or 0.57 pc at a distance of 1.8 kpc) and the maximum velocity separation of $14\,{\rm km\,s^{-1}}$, the dynamical age of the outflow was estimated to be 4.0×10^4 yr. The mass flow rate is then $8.8\times10^{-3}\,M_\odot\,{\rm yr^{-1}}$, which requires a driving engine with a bolometric luminosity $L_{\rm bol} \sim 1.5\times10^3\,L_\odot$ (Shepherd & Churchwell 1996), i.e., a spectral type of B2 or B3 (Panagia 1973). SMM1 with its HIRES bolometric luminosity of $3.7\times10^3\,L_\odot$ (see Sect. 3.1.1) is a promising driving source. In fact, higher resolution observations (Beuther et al. 2002a) revealed that the real engine of the CO outflow is one of the three sub-sources within SMM1.

4.4 Velocity Gradients

We found, from the NH_3 lines, that there exists a velocity gradient from SW to NE across the core, indicating an internal motion. The velocity increases monotonically from $-17.5\,{\rm km\,s^{-1}}$at (0″, 0″) to $-16.3\,{\rm km\,s^{-1}}$at (40″, 40″), which gives a gradient of $2.8\,{\rm km\,s^{-1}\,pc^{-1}}$, slightly larger than the typical rotation induced gradients of $1\,{\rm km\,s^{-1}\,pc^{-1}}$for molecular cloud cores (Goodman et al. 1993), but within the range found by Jijina et al. (1999) in their sample. The NH_3 line profile also shows weak wing emission. While the bipolar feature can be clearly seen in the velocity integrated intensity maps in Fig. 7a, the existence of the velocity gradients and the low velocity ($\sim 2\,{\rm km\,s^{-1}}$) outflowing gas are also evident in the position–velocity diagram in Fig. 7b. The existence of this outflowing gas complicates the interpretation of the observed velocity gradients. However, this is not likely to be the result of more independent sub cores with slightly different velocities inside the NH_3 core we observed, since the sub cores revealed by Beuther

et al. (2002a) are aligned almost perpendicular to the gradient discussed here. Therefore, the observed gradients could be a combined effect of the outflow and the core rotation.

4.5 Photometric Variabilities

Variability in low-mass protostars has been studied by Hartmann (1998), and large optical variability has been observed in FU Orionis type objects (Bell et al. 1995, and reference therein) and Herbig Ae/Be stars (Herbst & Shevchenko 1999). The NIR variations could be caused by starspots modulation, extinction variations, and accretion variations, or more probably, by all three acting simultaneously.

Among the sources showing variabilities (see Table 2), PCS–IR 2 and –IR 3 have optical counterparts with small extinction. Large extinctions ($A_\mathrm{v} > 14$) are found for the rest, indicating their embedded nature. PCS–IR 81 is a NIR nebula (PCS) and there may exist large discrepancies between the different photometric systems since the source is extended. PCS–IR 39, 40 belong to the SW cluster and both show evidence that the variabilities are stronger at shorter wavelengths than at longer ones, implying large variability in optical wavelengths. Unfortunately, both PCS–IR 39, 40 are labelled as undetected in K_s in the 2MASS catalog, because their K_s band photometric errors were not determined. Based on a mass of $4\,M_\odot$ (PCS) and a spectral type of B8 from its color-magnitude diagram, we conclude that PCS–IR 40 is likely to be a Herbig Ae/Be star. Large optical variability is known to be present in Herbig Ae/Be stars later than B8 (Herbst & Shevchenko 1999). PCS–IR 93 is the only star showing possible presence of circumstellar material from its location in the $J - H/H - K_\mathrm{s}$ color-color diagram (not shown here). Neither the PCS nor the 2MASS detected this source in the J band. Interestingly, the source IR 93 appeared to be highly polarized (Jiang et al. 2001), indicating its nebulosity nature. Beuther et al. (2002a) further argued that the object labelled mm1 in their paper is the exciting source of this nebula. Given the point like feature, it does not seem likely that the large difference between the PCS and 2MASS data is caused by photometric inaccuracy. What could cause the large variation in NIR magnitudes if the source PCS–IR93 is not a star but a nebula? An alternative possibility is that underlying this nebula there is a star which is indeed the source of the NIR variation we are seeing here. Although the type of this star can not be determined from the color-magnitude diagram because it is not detected in the J band, it does not look like an intermediate or high mass star as judged from its H and K_s magnitudes. It is possible that we are seeing an FU Orionis type of behavior in this star.

4.6 The Clustering Star Formation

Overall, the region appears to be a group of five NIR clusters within a radius of $30'$ from I 05358 (see table 1 in Bica et al. 2003 and references therein). Except the one associated with SMM1, i.e. the NE cluster in S 233 IR (PCS, Jiang et al. 2001), the other four clusters are all associated with IRAS sources, namely, I 05358 inside the SW cluster of S 233 IR (PCS, Jiang et al. 2001), IRAS 05361+3539 inside G173.58+2.45 (Shepherd & Watson 2002, labelled as I 05361 in Fig. 1), IRAS 05375+3540 inside S235B (Carpenter et al. 1993; Hoddap et al. 1994, I 05375 in Fig. 1), IRAS05377+3548 inside S235 (Carpenter et al. 1993, I 05377 in Fig. 1).

The core averaged intrinsic NH_3 line width of $2.19\,\mathrm{km\,s^{-1}}$ is found to be predominantly contributed by non-thermal turbulence with the nonthermal line width $\Delta\,v_\mathrm{NT}$ of about $2.18\,\mathrm{km\,s^{-1}}$. Further supported by its substantial mass, this core is reminiscent of the "turbulent, massive dense cores" forming clusters or groups of stars in the Jijina samples (samples IV and V in Jijina et al. 1999).

Are these clusters physically related? Or, in other words, is there a large scale chain of star formation across the whole region? Such questions are of obvious interest to an understanding of the mode of massive star formation, but more molecular line observations are needed to answer these questions.

4.7 Star Formation Efficiency

Star formation efficiency (SFE), defined as the ratio of the total stellar mass to the total combined mass of stars and gas, is used as a measure of star formation activity in a cloud (e.g. Wilking & Lada 1983). It is a fundamental parameter of both the star and cluster formation processes. The SFE is different in different clouds and the SFE of a cluster increases with time and typically can reach a maximum value of 30% by the time the cluster emerges from its parental cloud cores (Lada & Lada 2003). The Orion Trapezium cluster has an SFE of 30%, while in Serpens and Rho Oph, SFE $\sim$10%.

Taking the stellar masses estimated for the cluster members defined by the PCS, we obtained a total stellar mass of 10.7 $M_\odot$ in the NE cluster and 38.4 $M_\odot$ in the SW cluster. We then obtained an SFE of $\sim$4% for the NE cluster, and one of 47% for the SW cluster. For the region as a whole, the overall average SFE is about 11%. It is important to note that underestimates may be involved here. The PCS has an estimated mass completeness limit of 0.2 $M_\odot$ for the SW cluster and of 1 $M_\odot$ for the NE cluster. As we have learned from the IMF of the Trapezium cluster, there is a broad peak extending roughly from 0.6 to 0.1 $M_\odot$. We can therefore conclude that the SFE of the NE cluster is definitely greater than $\sim$4%. However, for the SW cluster, this underestimate may be balanced or even overbalanced by the fact that the dust properties in the SW cluster can be very different from those in the NE cluster. The mass estimate based on the dust properties of the NE clusters is likely to have underestimated the core mass of the SW cluster (e.g. κ_{870} could be lower for its low density). Although these SFE measurements are still quite uncertain (mainly due to the large uncertainties in the determinations of both the stellar and gaseous mass within a core), the large contrast of the SFE values in the two clusters suggests that the NE cluster is less evolved than the SW cluster, in line with the other pieces of evidence already mentioned.

The significant (sub)millimeter flux and the dense molecular core argue for a source in an early stage. However, the 20–25 μm MIR excess, if it is associated with the main (sub)millimeter core, indicates an evolutionary stage later than class–0 sources. This is further supported by the fact that the ratio of $L_{\rm bol}/(10^3 L_{1.3\,\rm mm})$ of SMM1 is $\sim$50, a value within the range for the class–I objects (André et al. 1993). However, given the fact that SMM1 contains multiple sources (Beuther et al. 2002a), the existence of younger sources is still possible.

5 CONCLUSIONS

1. Four submillimeter dust emission sources are revealed in the massive star forming region S 233 IR. The main core SMM1 is associated with the NE cluster, while a weaker source SMM2 coincides with the SW cluster. The best fit of the SED of the main core SMM1 gives an emissivity of β=1.6, and temperatures of 32K and 92 K for the cold– and hot–dust components, respectively. The SMM1 core mass is 246 $M_\odot$ and the total mass is 440 $M_\odot$.
2. CO J = 3–2 molecular outflow lobes were detected to be centered on the dense dust core but not the IRAS source. Low velocity bipolar outflows were also seen in NH_3 (1,1) emission. There is a good agreement between our results and all the recent high resolution

molecular line observations and NIR polarization results. The total mass of the CO outflow is estimated to be $35\,M_{\odot}$.

3. SMM1 is found to have a temperature gradient decreasing from inside out, indicative of the presence of interior heating sources. The non-thermally dominated NH_3 line width as well as the substantial core mass further suggest the SMM1 core is a "turbulent, massive dense core", that is in the course of forming a cluster or group of stars.
4. Near infrared photometric variations are found for a number of the stars. The variations of the star PCS–IR 40 are likely to be the counterpart of large optical variation of a B8 type Herbig Ae/Be star. The large variation found in PCS–IR 93, a previously found highly polarized nebula, is most likely from the underlying star showing possibly FU Orionis type of behavior.
5. SFE is found to be much higher in the SW cluster than in the NE cluster. This further supports the view that the SW cluster is more evolved than the NE cluster.
6. The mid infrared excess and the value of $L_{\rm bol}/(10^3 L_{1.3\,\rm mm})$ $\sim$50 for SMM 1 indicate its overall class–I feature. The existence of younger sources (i.e. class–0s) inside the core is still possible.

Acknowledgements The authors wish to thank Drs. C. Henkel and M. Miller, the HHT staffs and Effelsberg operators for their help in the data acquisition and reduction. We appreciate Dr. Beuther for providing us with the IRAM–30 m 1200 μm continuum map. We also benefited from discussions with Drs. Z.-B. Jiang and Y.-F. Chen. This paper makes use of data products from the Two Micron All Sky Survey, which is a joint project of the University of Massachusetts and Infrared Processing and Analysis Center, funded by the National Aeronautics and Space Administration and the National Science Foundation. R.Q.M. acknowledges support by the exchange program between the Chinese Academy of Sciences and the Max-Planck-Gesellschaft and hospitality of Max Planck Institut für Radioastronomie (MPIfR). This work was supported in part by NSFC grants 10373025, 10133020 and CMST grant G19990754.

References

André P., Ward–Thompson D., Barsony M., 1993, ApJ, 406, 122

Beichmann C. A., Negebauer G., Habing H. J. et al., 1987, IRAS Explanatory Supplement

Bell K. R., Lin D. N. C., Hartmann L. W., Kenyon S. J., 1995, ApJ, 444, 376

Beuther H., Schilke P., Gueth F., McCaughrean M., Andersen M., Sridharan T. K., Menten K. M., 2002a, A&A, 387, 931

Beuther H., Schilke P., Menten K. M., Motte F., Sridharan T. K., Wyrowski F., 2002b, ApJ, 566, 945

Bica E., Dutra C. M., Barbuy B., 2003, A&A, 397, 177

Cabrit S., Bertout C., 1990, ApJ, 348, 530

Carpenter J. M., Snell R. L., Schloerb F. P., Skrutskie M. F., 1993, ApJ, 407, 657

Cesaroni R., Felli M., Walmsley C. M., 1999, A&AS, 136, 333

Choi M., Evans N. J. II, Jaffe D. T., 1993, ApJ, 417, 624

Downes D., 1989, Evolution of Galaxies – Astronomical Observations, Lecture Notes in Physics 333, eds. I. Appenzeller, H. Habing, P. Lena, Berlin: Springer Verlag, p.353

Goodman A. A., Benson P. J., Fuller G. A., Myers P. C., 1993, ApJ, 406, 528

Harju J., Walmsley C. M., Wouterloot J. G. A., 1993, A&AS, 98, 51

Hartmann L., Calvet N., Gullbring E., DÁlessio P., 1998 ApJ, 495, 385

Herbst W., Shevchenko V. S., 1999, AJ, 118, 1043
Hildebrand R. H., 1983, QJRAS, 24, 267
Ho P. T. P., Townes C. H., 1983, ARA&A, 21, 239
Hodapp K.-W., 1994, ApJS, 94, 615
Jiang Z.-B., Yao Y.-Q., Yang J., Ishii M., Nagata T., Nakaya H., Sato S., 2001, AJ, 122, 313
Jijina J., Myers P. C., Adams F. C., 1999, ApJS, 125, 161
Kerton C. R., Martin P. G., Johnstone D., Ballantyne D. R., 2001, ApJ, 552, 601
Lada C. J., Lada E. A., 2003, ARA&A, 41, 57
Mao R.-Q., PhD thesis, Purple Mountain Observatory, CAS, 1999
Mao R.-Q., Yang J., Henkel C., Jiang Z. B., 2002, A&A, 389, 589
Menten K., 1991, ApJ, 180, L75
Panagia N., 1973, ApJ, 78, 929
Porras A., Cruz-Gonzáles I., Salas L., 2000, A&A, 361, 660 (PCS)
Shepherd D. S., Churchwell E., 1996, ApJ, 472, 225
Shepherd D. S., Watson A. M., 2002, ApJ, 566, 966
Snell R. L., Dickman R. L., Huang Y. L., 1990, ApJ, 352, 139
Szymczak M., Hrynek G., Kus A. J., 2000, A&AS, 143, 653
Tofani G., Felli M., Taylor G. B., Hunter T. R., 1995, A&AS, 112, 299
Wilking B. A., Lada C. J., 1983, ApJ, 274, 698